Inverse design of higher-order photonic topological insulators

Yafeng Chen,[1,2] Fei Meng,[2] Yuri Kivshar,[3] Baohua Jia,[2] and Xiaodong Huang [2,*]

[1]*Key Laboratory of Advanced Technology for Vehicle Body Design & Manufacture, Hunan University, Changsha 410082, China*
[2]*Centre of Translational Atomaterials (CTAM), Faculty of Science, Engineering and Technology, Swinburne University of Technology, Hawthorn VIC 3122, Australia*
[3]*Nonlinear Physics Center, Research School of Physics, Australian National University, Canberra ACT 2601, Australia*

(Received 3 February 2020; accepted 6 April 2020; published 1 May 2020)

The recently discovered second-order photonic topological insulators (SPTIs) are characterized by gapped edge states and robust corner states, and they provide novel approaches to the traditional ways to manipulate light. In a general case, the overlapped band gap of nontrivial and trivial photonic crystals composing SPTIs is narrow, which barely allows for the production of strongly localized states. Here, we introduce an intelligent numerical approach for the inverse design of large classes of SPTIs with great flexibility for controlling the properties of topological edge and corner states. In the optimized designs, the overlapped band gap of the nontrivial and trivial photonic crystals substantially exceeds that of the existing SPTIs, and it enables the existence of highly localized corner and edge states with nearly flat dispersion. We design several structures supporting both topological edge and corner states at the desired frequencies. Through programming newly created SPTIs, we suggest a strategy for routing topological edge and corner states. Our findings pave the way for the development of integrated photonic devices with topological protection and innovative functionalities.

DOI: 10.1103/PhysRevResearch.2.023115

I. INTRODUCTION

The discovery of topological phases opened up new horizons in the study of condensed-matter physics [1–6]. Topological insulators with robust gapless edge states were expected to deliver a broad range of applications ranging from spintronics to quantum computation [7–9]. Recently, the concept of topological phases has entered the realm of photonics [10–14], revolutionizing some of the traditional views on light manipulation and light-matter interaction. Many novel photonic devices, such as backscattering-immune sharply bent waveguides [15], spin-polarized switches [16], robust delay lines [17], nonreciprocal devices [18], and topological laser [19,20], have been predicted and demonstrated in experiment. Recently, a novel type of so-called second-order topological insulator featuring gapped edge states and in-gap corner/hinge states has been proposed in the field of electronics [21–25], and it was then extended to photonic systems [26,27]. The second-order corner states of photonic crystals (PCs) [28–30] have been experimentally verified, and the photonic crystal nanocavity with a high Q factor based on a topological corner state has been demonstrated [31].

The occurrence of topological states and corner states depends on the spatial distribution of the constituent material within the unit cell of trivial and nontrivial photonic crystals. The existing designs of second-order photonic topological insulators (SPTIs) mainly relies on the trial-and-error approach. The resulting properties of the topological insulators may be far from optimum. For instance, the overlapped band gap of nontrivial and trivial PCs is relatively narrow and barely produces strongly localized topological edge and corner states. Topological photonics provides an unprecedented means for developing next-generation integrated photonic devices [10], ranging from optical interconnects [32] to quantum technologies [33]. One of the key elements of integrated photonic devices is the wavelength router, which separates light with various wavelengths into different channels and dramatically increases the data capacity in a fiber or waveguide [34,35]. However, wavelength routers utilizing topological edge and corner states have never been predicted and explored. The design of wavelength routers requires that topological edge and corner states occur at various frequency levels, which creates a challenge for the current design approach.

This paper presents an intelligent topology optimization approach for designing SPTIs and other types of higher-order topological structures. We uncover the procedure to achieve the overlapped band gap of the created nontrivial and trivial PCs for more than twice that of the current SPTI designs, and we demonstrate highly localized corner states and an edge state with nearly flat dispersion. In addition, the proposed approach provides great flexibility for tuning the operating frequencies of the topological edge and corner states. By programming newly created SPTIs, we demonstrate high-performance four-channel photonic routers for topological edge states and three-channel photonic routers for topological corner states.

*Author to whom all correspondence should be addressed: xhuang@swin.edu.au

II. INVERSE-DESIGN APPROACH

Topology optimization employs a robust numerical algorithm to seek the layout of materials within the design domain, so as to minimize or maximize the defined objective function [36]. Topology optimization has been proven to be an efficient and effective tool for the design of PCs [37–46]. Here, we will extend topology optimization to design the unit cell of nontrivial and trivial PCs for SPTIs. The 2D hexagonal unit cells of PCs are made of silicon (the relative permittivity, $\varepsilon = 12$) with C_{6v} symmetry. The lattice constant is a, and the frequency is normalized as $\Omega = \omega a/2\pi c$, where c denotes the speed of light in vacuum. The transverse magnetic (TM) mode is assumed, where the magnetic field is confined in the xy plane and the electric field is perpendicular to the plane.

Topology optimization first constructs a nontrivial PC (NP), which has two dipolar modes located above two quadrupolar modes in the band diagram. The unit cell is discretized with N finite elements, and the design variables, x_e $(e = 1, 2, \ldots, N)$, are the artificial densities of elements in the unit cell. $x_e = 0$ denotes that element e is full of air and $x_e = 1$ for the specified dielectric material, e.g., silicon in our examples. The optimization objective is to find the optimal discrete values of x_e, so that the dipolar modes and quadrupolar modes occur at the specified frequencies, ω_1 and ω_2 $(\omega_1 > \omega_2)$. The specific resonant mode at the specified frequency can be excited by maximizing the frequency-averaged local density of states (LDOS) [41,47,48], $\tilde{f}(\omega, \mathbf{J}, \mathbf{E})$, emitted from a harmonic current source, $\mathbf{J}$. The electric field, $\mathbf{E}$, is the solution of the steady-state Maxwell equation, $\nabla \times (1/\mu)\nabla \times \mathbf{E} - \varepsilon(\mathbf{r})\omega^2\mathbf{E} = i\omega\mathbf{J}$. The current J is judiciously constructed in the Supplemental Material [59], Sec. 1, to excite the dipolar and quadrupolar modes, respectively. To solve it mathematically, the problem is converted to the topology optimization formulation with objective and constraint functions as follows:

$$\begin{aligned} &\text{Find}: \; x_e \; (e = 1,\; 2,\; \ldots,\; N) \\ &\min : t \\ &\text{s.t.} \;:\; t \geqslant \frac{1}{\tilde{f}_1(\omega_1,\; \mathbf{J}_1,\; \mathbf{E}_1)}, \quad t \geqslant \frac{1}{\tilde{f}_2(\omega_2,\; \mathbf{J}_2,\; \mathbf{E}_2)} \\ &\quad x_e \in \{0,\, 1\}. \end{aligned} \tag{1}$$

$\tilde{f}_1$ and $\tilde{f}_2$ are the frequency-averaged LDOS for the dipolar and quadrupolar modes, respectively. The details on topology optimization can be found in the Supplemental Material [59].

By gradually modifying the targeted frequencies of dipolar and quadrupolar modes, we obtain a nontrivial PC (denoted as NP1) as shown in Fig. 1(a), with a wide band gap between $\Omega = 0.433$ and 0.620 in Fig. 1(b). The insets in Fig. 1(b) illustrate that the two dipolar modes, p_x/p_y, are located above the two quadrupolar modes, $d_{x^2-y^2}/d_{xy}$, at Γ. Such a parity-inverse band order indicates that the band gap is nontrivial [16,18]. Next, we create a trivial PC (denoted as TP) by topology optimization [49], which aims to maximize the band gap between the second band and the third band. The optimized unit cell and its band diagram are given in Figs. 1(c) and 1(d), respectively, and its band gap ranges from $\Omega = 0.434$ to 0.583. The overlapped band-gap width between the nontrivial and trivial PCs achieves 29.3%, which is more than twice that compared with those of the intuitive

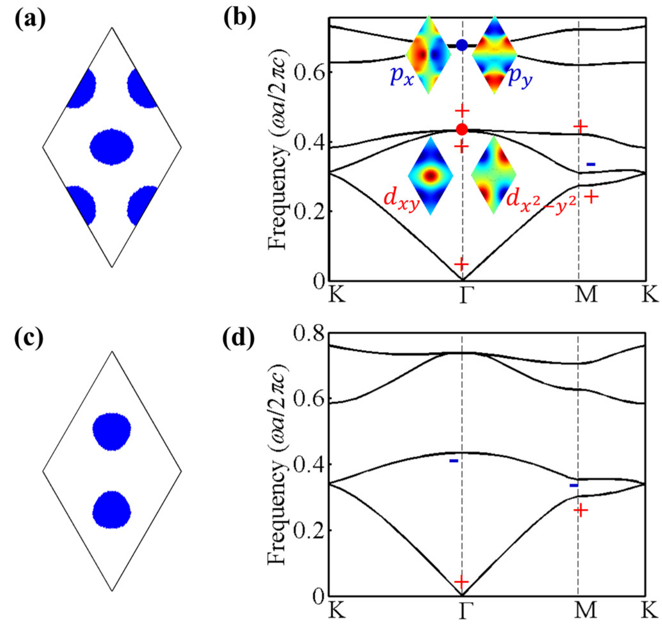

FIG. 1. Optimized primitive unit cell for topological (a) nontrivial PC and (c) trivial PC. Parts (b) and (d) are band diagrams for topological nontrivial PC and trivial PC, respectively. The insets are electric-field profiles of dipolar and quadrupolar modes at the Γ point.

SPTIs in Refs. [28,29,31]. Such a wide overlapped band gap enables highly localized edge and corner states, and is a key to providing the programming room for potential applications.

Here, we use the bulk polarization to confirm the topological properties of the optimized PCs. Because of the C_{6v} symmetry, the bulk polarization $\mathbf{P} = (P_x, P_y)$ can be calculated by the parities at high symmetric points through [25,50–52]

$$P_x = P_y = \frac{1}{2}\left(\sum_n q_n \bmod 2\right), \qquad (-1)^{q_n} = \frac{\eta_n(M)}{\eta_n(\Gamma)}, \tag{2}$$

where $i = x, y$ stands for the direction; η_n denotes the parity at the high-symmetry point for the nth band, which means even- or odd-symmetry behavior under inversion at the C_{6v} point group center. The p modes have an odd parity $(-)$, while the d and s modes have an even parity $(+)$. The parities at high symmetric points are labeled in the band diagrams. Derived from Eq. (2), the bulk polarization for NP1 equals (1/2,1/2), which ascertains that NP1 is in a topological nontrivial phase. The bulk polarization for TP is (0,0), which confirms that TP is in a topological trivial phase.

It is noticed that the design of NP1 is similar to the perturbed kagome lattice for the quantum spin Hall effect-based photonic topological insulator [16]. The design of TP is the same as that of the honeycomb lattice with the Dirac cone at K, which is used as a precursor to create the quantum valley Hall effect-based photonic topological insulator [53]. However, the topological mechanism exploited here is based on topological polarization and thus is fundamentally different from the Chern-related quantum valley/spin Hall effect [54].

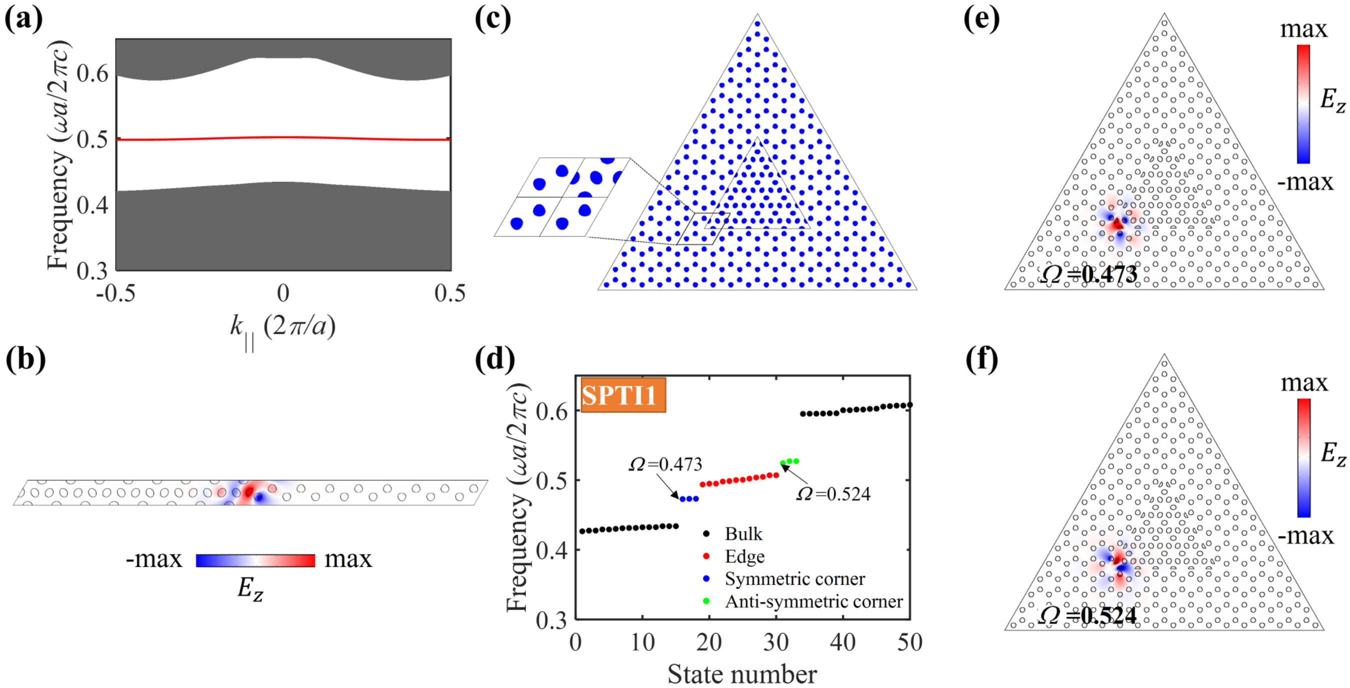

FIG. 2. (a) Band diagram for a supercell with a domain wall between 8 NP1s and 8 TPs as shown in (b); (b) distribution of the electric field for a 1D edge state at Γ; (c) metastructure constructed by NP1s and TPs for the calculation of corner states; (d) eigenfrequencies of the metastructure in (c); (e) distribution of the electric field for a symmetric corner state; and (f) distribution of the electric field for an antisymmetric corner state.

III. TOPOLOGICAL EDGE AND CORNER STATES

According to the bulk-boundary correspondence principle [55,56], topological edge states emerge at the interface between trivial and nontrivial PCs. To demonstrate the topological edge states, a supercell composed of eight unit cells of NP1 and eight unit cells of TP is constructed with a domain wall as indicated in Fig. 2(b). The numerical simulation is performed in COMSOL MULTIPHYSICS. Figure 2(a) presents the projected band diagram. It can be seen that one edge state with almost flat dispersion occurs inside the overlapped band gap of NP1 and TP. The mode profile at Γ [Fig. 2(b)] reveals that the electric field is highly localized at the interface and is decayed exponentially into the bulk. The group index for this edge state is larger than 60, indicating the slow light propagation, which has many potential applications in nonlinear optics [57]. However, such a gapped 1D edge state is fundamentally different from the gapless 1D edge state in topological photonic crystals based on quantum spin Hall effects (QSHEs) [58]. The gapped edge state is also a prerequisite for the realization of a 0D corner state [28,29]. To confirm the existence of a 0D corner state, we construct a triangle metastructure, as shown in Fig. 2(c), with NP1 at the center and TP at the surrounding. Figure 2(d) displays the eigenfrequencies of the metastructure. Different from the existing SPTIs [26–29] with symmetric corner states only, we observe three near-degenerate symmetric corner states (blue dots) and three antisymmetric corner states (green dots). The diagonal mirror plane is the angular bisector of the corner. These in-gap symmetric and antisymmetric corner states emerge at the frequencies between the 1D edge states (red dots) and the bulk bands (black dots). Figures 2(e) and 2(f) show the electric-field distribution for the symmetric corner state and the antisymmetric corner state, respectively. They clearly show that the electric field is highly localized symmetrically or antisymmetrically at the corner. The symmetric corner mode supports a high-Q factor with 1.3×10^6, which significantly exceeds that in Ref. [26]. Note that the finite Q-factor corresponds to the in-plane leakiness of the mode, calculated here by employing scattering boundary conditions for the two-dimensional simulations.

IV. TUNING FREQUENCIES OF THE EDGE AND CORNER STATES

By specifying different frequencies of quadrupolar modes in topology optimization, various optimized nontrivial PCs can be obtained. Figure 3(a) shows four different nontrivial PCs by specifying the normalized frequency of quadrupolar modes at 0.440, 0.450, 0.470, and 0.485, respectively. These optimized nontrivial PCs are denoted as NP2, NP3, NP4, and NP5, respectively. Thus, five SPTIs (SPTI1, SPTI2, SPTI3, SPTI4, and SPTI5) can be created by assembling these optimized nontrivial PCs with a TP. Figure 3(b) shows superimposed projected band diagrams for the supercells of SPTI1, SPTI3, SPTI4, and SPTI5, demonstrating that the edge states of these SPTIs occur at different frequencies. These edge states occur at the overlapped band gap between $\Omega = 0.485$ and 0.588. Figures 3(c) and 3(d) show the eigenfrequencies of the metastructures, which are similar to the one shown in Fig. 2(c) except for replacing NP1 with NP2 and NP3, respectively. It can be seen from Figs. 2(d), 3(c), and 3(d)

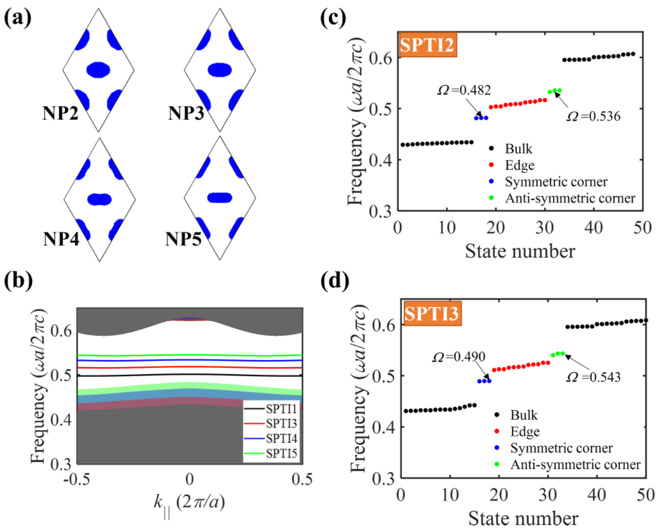

FIG. 3. (a) Optimized nontrivial PCs by specifying the normalized frequency of quadrupolar modes at 0.440, 0.450, 0.470, and 0.485, respectively; (b) superimposed projected band diagrams for SPTI1, SPTI3, SPTI4, and SPTI5; (c) eigenfrequencies of the metastructure shown in Fig. 2(c) by replacing NP1 with NP2; and (d) eigenfrequencies of the metastructure shown in Fig. 2(c) by replacing NP1 with NP3.

that the SPTI1, SPTI2, and SPTI3 metastructures have corner states at different frequencies.

V. ROUTING TOPOLOGICAL EDGE AND CORNER STATES

Through the analysis of topological edge and corner states in the previous section, routing topological edge and corner states with different frequencies can be achieved by purposely programming these optimized NPs and TPs. As an example, Fig. 4(a) shows the programming diagram of a photonic device composed of NP1, NP3, NP4, NP5, and two pieces of TPs with six channels (boundaries), which aims at manipulating waves with normalized frequencies ranging from 0.485 to 0.588. Since the supercell of two nontrivial PCs exhibits the band gap without any edge states (see the Supplemental Material [59], Sec. 2), two channels between NP1 and NP5, and NP3 and NP4, are blind. The other four channels between nontrivial and trivial PCs, as highlighted by the colored lines, will be utilized for the propagation of light waves due to the existence of edge states. As shown in Fig. 3(b), these four channels support edge states at different frequencies, which do not interfere with each other. As a result, light waves with different frequencies emitting from a line source at the center of the device (denoted by the red asterisk) may propagate along different channels. Figures 4(b)–4(e) show the distributions of the electric field when the source has the normalized frequency 0.502, 0.517, 0.536, and 0.546, respectively. It can be seen that topological edge states with different frequencies are routed into different channels. Figure 4(f) presents the spectrum of normalized transmission for the ports at the end of each channel. It can be seen that, when the

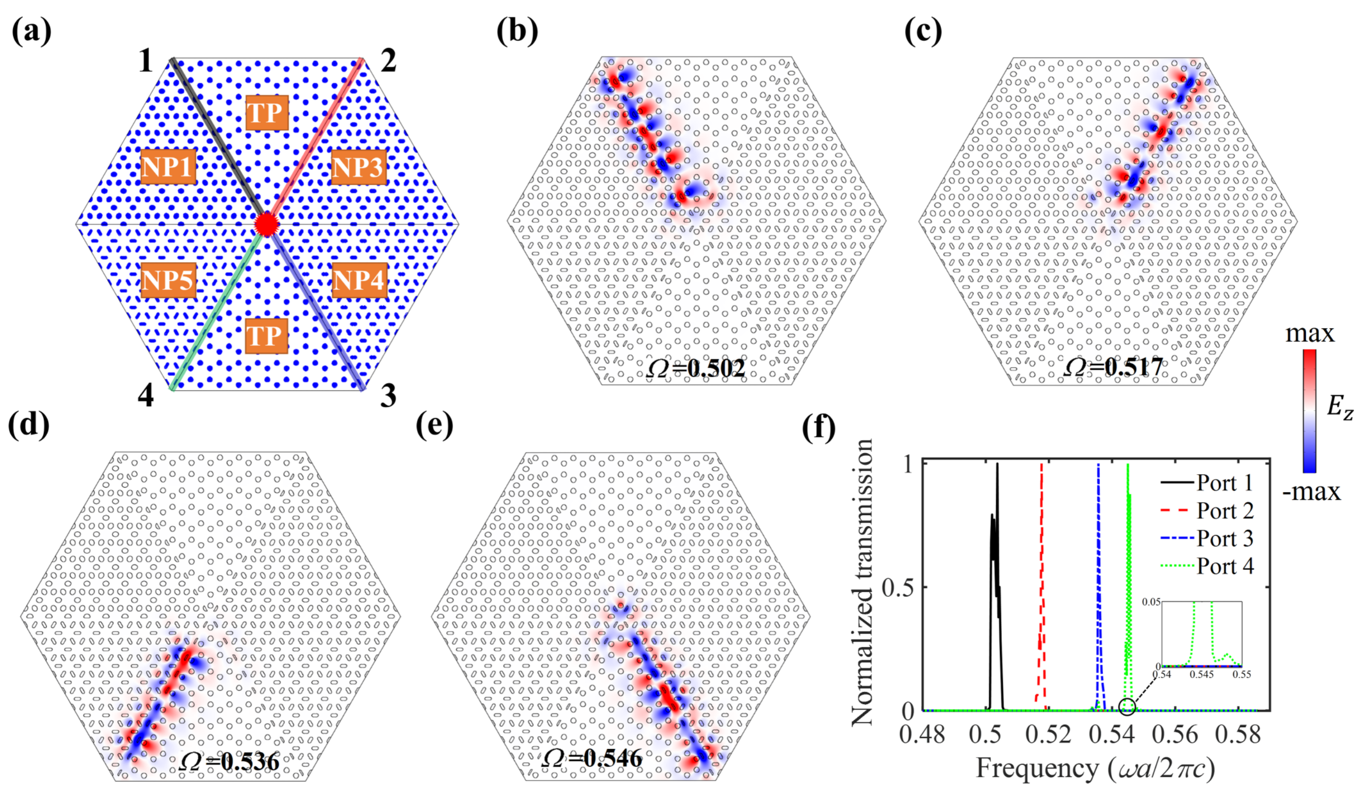

FIG. 4. Routing topological edge states with different frequencies. (a) Schematic of the photonic device for routing topological edge states. Color lines mark four channels formed between nontrivial PCs and trivial PCs. (b), (c), (d), and (e) Simulated electric-field distribution for the point source with the normalized frequency being 0.502, 0.517, 0.536, and 0.546, respectively. (f) Spectrum of normalized electric field for the ports at the end of each channel.

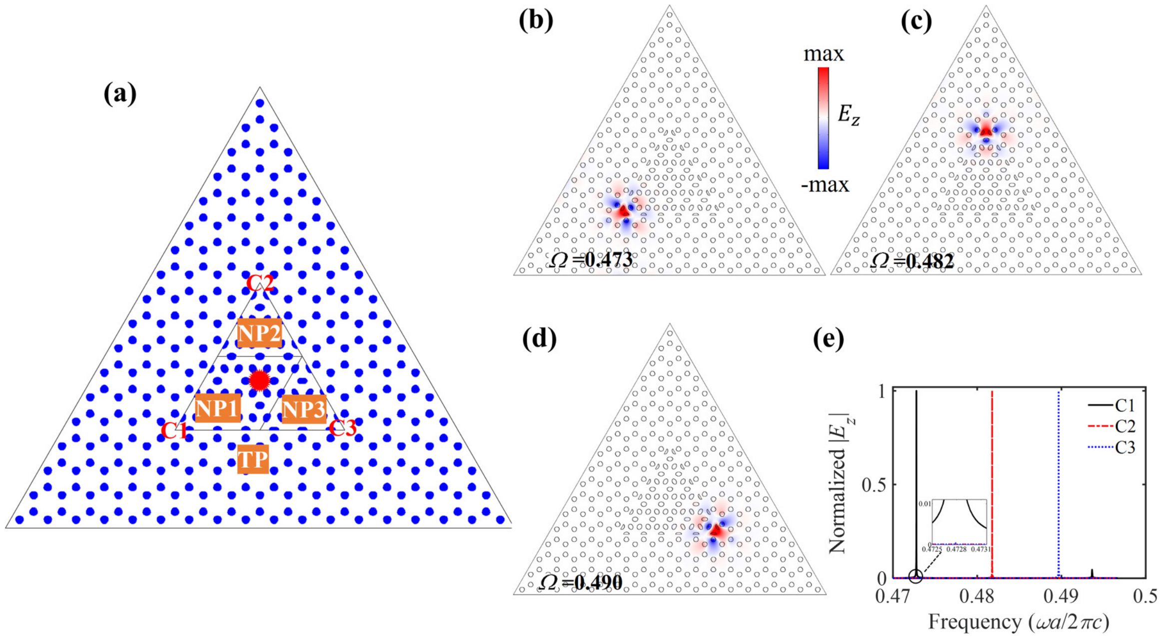

FIG. 5. Routing topological corner states with different frequencies. (a) Schematic of the photonic device for routing topological corner states. (b)–(d) Numerically simulated electric-field distribution for the line source with the normalized frequency being 0.473, 0.482, and 0.490, respectively. (e) Spectrum of normalized electric field at the corners.

electric field at the port of one channel reaches its peak, the electric fields at other ports are nearly zero. The calculated cross-talks are below −60 dB. Therefore, a high-performance four-channel wavelength demultiplexer for topological edge states is successfully demonstrated.

Figure 5(a) illustrates the schematic diagram of another programming diagram of a photonic device for routing topological corner states. The device consists of three different nontrivial PCs—NP1, NP2, and NP3—surrounded by a TP. Three 60° corners are formed between each nontrivial PC and the trivial PC, and they are denoted as C1, C2, and C3, respectively. These corners possess different frequencies of the symmetric corner states, which can be seen in Figs. 2(d), 3(c), and 3(d). We put a line source, the same as that in [28], at the center of the internal triangle region for nontrivial PCs, as denoted by the red asterisk. The boundary of the metastructure in Fig. 5(a) is set as the scattering boundary condition. Figures 5(b)–5(d) show the simulated electric-field distribution for the point source with the normalized frequency being 0.473, 0.482, and 0.490, corresponding to the frequency of the symmetric corner state for each corner, respectively. It can be seen that by changing the frequency of the point source, the corner states at different corners are selectively excited, and the electric field is highly localized at different corner. Figure 5(e) presents the spectrum of the normalized electric field for each corner. It is shown that when one corner is excited, the electric fields of other corners are nearly zero. Therefore, the photonic demultiplexer for topological symmetric corner states is successfully demonstrated. Routing antisymmetric topological corner states is shown in the Supplemental Material (SM) [59], Sec. 3. In addition, we demonstrate the robustness of corner states against perturbations in Sec. 4 of the SM, confirming that the topological corner state possesses a good immunity against defects. In Sec. 5 of the SM, we discuss the feasibility of an experimental realization of the corner router.

VI. CONCLUSIONS

We have proposed an intelligent method for applying an inverse design to high-order topological insulators, and we demonstrated our method for the example of SPTIs. We demonstrated how to achieve an overlapped band gap of nontrivial and trivial PCs that is more than twice as large as that for the existing SPTI structures, which enables the existence of highly localized corner and edge states with nearly flat dispersion. The group index for the edge state is larger than 60, indicating slow light propagation, which has many potential applications in nonlinear optics. By inversely designing several SPTIs with different frequencies for both edge and corner states and purposely programming the SPTIs, we have demonstrated high-performance four-channel photonic routers for topological edge states and three-channel photonic routers for corner states. Our findings provide great flexibility for utilizing topological edge and corner states in photonic applications, which is of great importance in developing photonic devices with topological protection and novel functionalities.

ACKNOWLEDGMENTS

The work was supported by the Australian Research Council (Grants No. FT130101094 and No. DP200101168). Y.C. acknowledges support from China Scholarship Council.

[1] D. J. Thouless, M. Kohmoto, M. P. Nightingale, and M. den Nijs, Quantized Hall Conductance in a Two-Dimensional Periodic Potential, Phys. Rev. Lett. **49**, 405 (1982).
[2] F. D. M. Haldane, Fractional Quantization of the Hall Effect: A Hierarchy of Incompressible Quantum Fluid States, Phys. Rev. Lett. **51**, 605 (1983).
[3] F. D. M. Haldane, Model for a Quantum Hall Effect without Landau Levels: Condensed-Matter Realization of the "Parity Anomaly," Phys. Rev. Lett. **61**, 2015 (1988).
[4] Y. Hatsugai, Chern Number and Edge States in the Integer Quantum Hall Effect, Phys. Rev. Lett. **71**, 3697 (1993).
[5] C. L. Kane and E. J. Mele, Quantum Spin Hall Effect in Graphene, Phys. Rev. Lett. **95**, 226801 (2005).
[6] C.-Z. Chang *et al.*, Experimental observation of the quantum anomalous Hall effect in a magnetic topological insulator, Science **340**, 167 (2013).
[7] M. Z. Hasan and C. L. Kane, Colloquium: topological insulators, Rev. Mod. Phys. **82**, 3045 (2010).
[8] X.-L. Qi and S.-C. Zhang, Topological insulators and superconductors, Rev. Mod. Phys. **83**, 1057 (2011).
[9] H. Weng, R. Yu, X. Hu, X. Dai, and Z. Fang, Quantum anomalous Hall effect and related topological electronic states, Adv. Phys. **64**, 227 (2015).
[10] A. B. Khanikaev and G. Shvets, Two-dimensional topological photonics, Nat. Photon. **11**, 763 (2017).
[11] F. Haldane and S. Raghu, Possible Realization of Directional Optical Waveguides in Photonic Crystals with Broken Time-Reversal Symmetry, Phys. Rev. Lett. **100**, 013904 (2008).
[12] L. Lu, J. D. Joannopoulos, and M. Soljačić, Topological photonics, Nat. Photon. **8**, 821 (2014).
[13] L. Lu, J. D. Joannopoulos, and M. Soljačić, Topological states in photonic systems, Nat. Phys. **12**, 626 (2016).
[14] T. Ozawa *et al.*, Topological photonics, Rev. Mod. Phys. **91**, 015006 (2019).
[15] X. Cheng, C. Jouvaud, X. Ni, S. H. Mousavi, A. Z. Genack, and A. B. Khanikaev, Robust reconfigurable electromagnetic pathways within a photonic topological insulator, Nat. Mater. **15**, 542 (2016).
[16] L.-H. Wu and X. Hu, Scheme for Achieving a Topological Photonic Crystal by Using Dielectric Material, Phys. Rev. Lett. **114**, 223901 (2015).
[17] M. Hafezi, E. A. Demler, M. D. Lukin, and J. M. Taylor, Robust optical delay lines with topological protection, Nat. Phys. **7**, 907 (2011).
[18] Y. Yang, Y. F. Xu, T. Xu, H.-X. Wang, J.-H. Jiang, X. Hu, and Z. H. Hang, Visualization of a Unidirectional Electromagnetic Waveguide using Topological Photonic Crystals Made of Dielectric Materials, Phys. Rev. Lett. **120**, 217401 (2018).
[19] B. Bahari, A. Ndao, F. Vallini, A. El Amili, Y. Fainman, and B. Kanté, Nonreciprocal lasing in topological cavities of arbitrary geometries, Science **358**, 636 (2017).
[20] G. Harari, M. A. Bandres, Y. Lumer, M. C. Rechtsman, Y. D. Chong, M. Khajavikhan, D. N. Christodoulides, and M. Segev, Topological insulator laser: Theory, Science **359**, eaar4003 (2018).
[21] W. A. Benalcazar, B. A. Bernevig, and T. L. Hughes, Quantized electric multipole insulators, Science **357**, 61 (2017).
[22] J. Langbehn, Y. Peng, L. Trifunovic, F. von Oppen, and P. W. Brouwer, Reflection-Symmetric Second-Order Topological Insulators and Superconductors, Phys. Rev. Lett. **119**, 246401 (2017).
[23] Z. Song, Z. Fang, and C. Fang, (d−2)-Dimensional Edge States of Rotation Symmetry Protected Topological States, Phys. Rev. Lett. **119**, 246402 (2017).
[24] W. A. Benalcazar, B. A. Bernevig, and T. L. Hughes, Electric multipole moments, topological multipole moment pumping, and chiral hinge states in crystalline insulators,Phys. Rev. B **96**, 245115 (2017).
[25] C. Fang, M. J. Gilbert, and B. A. Bernevig, Bulk topological invariants in noninteracting point group symmetric insulators, Phys. Rev. B **86**, 115112 (2012).
[26] B.-Y. Xie, H.-F. Wang, H.-X. Wang, X.-Y. Zhu, J.-H. Jiang, M.-H. Lu, and Y.-F. Chen, Second-order photonic topological insulator with corner states, Phys. Rev. B **98**, 205147 (2018).
[27] J. Noh, W. A. Benalcazar, S. Huang, M. J. Collins, K. P. Chen, T. L. Hughes, and M. C. Rechtsman, Topological protection of photonic mid-gap defect modes, Nat. Photon. **12**, 408 (2018).
[28] B.-Y. Xie, G.-X. Su, H.-F. Wang, H. Su, X.-P. Shen, P. Zhan, M.-H. Lu, Z.-L. Wang, and Y.-F. Chen, Visualization of Higher-Order Topological Insulating Phases in Two-Dimensional Dielectric Photonic Crystals, Phys. Rev. Lett. **122**, 233903 (2019).
[29] X.-D. Chen, W.-M. Deng, F.-L. Shi, F.-L. Zhao, M. Chen, and J.-W. Dong, Direct Observation of Corner States in Second-Order Topological Photonic Crystal Slabs, Phys. Rev. Lett. **122**, 233902 (2019).
[30] A. El Hassan, F. K. Kunst, A. Moritz, G. Andler, E. J. Bergholtz, and M. Bourennane, Corner states of light in photonic waveguides, Nat. Photon. **13**, 697 (2019).
[31] Y. Ota, F. Liu, R. Katsumi, K. Watanabe, K. Wakabayashi, Y. Arakawa, and S. Iwamoto, Photonic crystal nanocavity based on a topological corner state, Optica **6**, 786 (2019).
[32] D. A. Miller, Attojoule optoelectronics for low-energy information processing and communications, J. Lightwave Technol. **35**, 346 (2017).
[33] P. Kok, W. J. Munro, K. Nemoto, T. C. Ralph, J. P. Dowling, and G. J. Milburn, Linear optical quantum computing with photonic qubits, Rev. Mod. Phys. **79**, 135 (2007).
[34] A. Y. Piggott, J. Lu, K. G. Lagoudakis, J. Petykiewicz, T. M. Babinec, and J. Vučković, Inverse design and demonstration of a compact and broadband on-chip wavelength demultiplexer, Nat. Photon. **9**, 374 (2015).
[35] L. Su, A. Y. Piggott, N. V. Sapra, J. Petykiewicz, and J. Vuckovic, Inverse design and demonstration of a compact on-chip narrowband three-channel wavelength demultiplexer, ACS Photon. **5**, 301 (2017).
[36] X. Huang and Y. Xie, *Evolutionary Topology Optimization of Continuum Structures: Methods and Applications* (Wiley, 2010).
[37] N. Bonod, S. Bidault, G. W. Burr, and M. Mivelle, Evolutionary optimization of all-dielectric magnetic nanoantennas, Adv. Opt. Mater. **7**, 1900121 (2019).
[38] W. Ma, F. Cheng, Y. H. Xu, Q. L. Wen, and Y. M. Liu, Probabilistic representation and inverse design of metamaterials based on a deep generative model with semi-supervised learning strategy, Adv. Mater. **31**, 1901111 (2019).
[39] Z. Lin, B. Groever, F. Capasso, A. W. Rodriguez, and M. Lončar, Topology-Optimized Multilayered Metaoptics, Phys. Rev. Appl. **9**, 044030 (2018).

[40] Z. Lin, L. Christakis, Y. Li, E. Mazur, A. W. Rodriguez, and M. Lončar, Topology-optimized dual-polarization Dirac cones, Phys. Rev. B **97**, 081408(R) (2018).

[41] Z. Lin, A. Pick, M. Lončar, and A. W. Rodriguez, Enhanced Spontaneous Emission at Third-Order Dirac Exceptional Points in Inverse-Designed Photonic Crystals, Phys. Rev. Lett. **117**, 107402 (2016).

[42] F. Meng, X. Huang, and B. Jia, Bi-directional evolutionary optimization for photonic band gap structures, J. Comput. Phys. **302**, 393 (2015).

[43] J. Huang *et al.*, Implementation of on-chip multi-channel focusing wavelength demultiplexer with regularized digital metamaterials, Nanophotonics **9**, 159 (2020).

[44] K. Yao, R. Unni, and Y. Zheng, Intelligent nanophotonics: Merging photonics and artificial intelligence at the nanoscale, Nanophotonics **8**, 339 (2019).

[45] S. Molesky, Z. Lin, A. Y. Piggott, W. Jin, J. Vucković, and A. W. Rodriguez, Inverse design in nanophotonics, Nat. Photon. **12**, 659 (2018).

[46] Z. Liu, X. Liu, Z. Xiao, C. Lu, H.-Q. Wang, Y. Wu, X. Hu, Y.-C. Liu, H. Zhang, and X. Zhang, Integrated nanophotonic wavelength router based on an intelligent algorithm, Optica **6**, 1367 (2019).

[47] X. Liang and S. G. Johnson, Formulation for scalable optimization of microcavities via the frequency-averaged local density of states, Opt. Express **21**, 30812 (2013).

[48] Y. Chen, F. Meng, G. Li, and X. Huang, Topology optimization of photonic crystals with exotic properties resulting from Dirac-like cones, Acta Mater. **164**, 377 (2019).

[49] F. Meng, Y. Li, S. Li, H. Lin, B. Jia, and X. Huang, Achieving large band gaps in 2D symmetric and asymmetric photonic crystals, J. Lightwave Technol. **35**, 1670 (2017).

[50] Z. Zhang, M. R. López, Y. Cheng, X. Liu, and J. Christensen, Non-Hermitian Sonic Second-Order Topological Insulator, Phys. Rev. Lett. **122**, 195501 (2019).

[51] Z. Zhang, H. Long, C. Liu, C. Shao, Y. Cheng, X. Liu, and J. Christensen, Deep-subwavelength holey acoustic second-order topological insulators, Adv. Mater. **31**, 1904682 (2019).

[52] F. Liu, M. Yamamoto, and K. Wakabayashi, Topological edge states of honeycomb lattices with zero berry curvature, J. Phys. Soc. Jpn. **86**, 123707 (2017).

[53] X.-D. Chen, F.-L. Zhao, M. Chen, and J.-W. Dong, Valley-contrasting physics in all-dielectric photonic crystals: Orbital angular momentum and topological propagation, Phys. Rev. B **96**, 020202 (2017).

[54] M. Saba, S. Wong, M. Elman, S. S. Oh, and O. Hess, Nature of topological protection in photonic spin and valley Hall insulators, Phys. Rev. B **101**, 054307 (2020).

[55] F. Liu, H.-Y. Deng, and K. Wakabayashi, Topological photonic crystals with zero Berry curvature, Phys. Rev. B **97**, 035442 (2018).

[56] L. Wang, R.-Y. Zhang, M. Xiao, D. Han, C. T. Chan, and W. Wen, The existence of topological edge states in honeycomb plasmonic lattices, New J. Phys. **18**, 103029 (2016).

[57] T. Baba, Slow light in photonic crystals, Nat. Photon. **2**, 465 (2008).

[58] A. B. Khanikaev, S. H. Mousavi, W.-K. Tse, M. Kargarian, A. H. MacDonald, and G. Shvets, Photonic topological insulators, Nat. Mater. **12**, 233 (2013).

[59] See Supplemental Material at http://link.aps.org/supplemental/10.1103/PhysRevResearch.2.023115 for detailed information on topology optimization formulations and the antisymmetric topological corner states.